RSC Advances

ROYAL SOCIETY OF CHEMISTRY

www.rsc.org/advances

Three-dimensional CoS_2/RGO hierarchical architecture as superior-capability anode for lithium ion batteries

Fei Fu, Yuanfu Chen, Pingjian Li*, Jiarui He, Zegao Wang, Wei Lin, and Wanli Zhang*

State Key Laboratory of Electronic Thin Films and Integrated Devices,
University of Electronic Science and Technology of China,
Chengdu 610054, PR China
E-mail: yfchen@uestc.edu.cn, lipingjian@uestc.edu.cn

Abstract

For the first time, three-dimensional hierarchical architecture of CoS_2/reduced graphene oxide (3DCG) with CoS_2 particles uniformly anchored on the graphene network has been synthesized by a facile hydrothermal method. The 3DCG anode exhibits superior electrochemical performances: it delivers a high reversible specific capacity of 1499 mAh g^{-1} and remains 1245 mAh g^{-1} after 150 cycles at a current density of 100 mA g^{-1}, which is the highest ever reported for CoS_2-based materials; the rate capability remains 306 mAh g^{-1} even at 4000 mA g^{-1}. The excellent performance can be attributed to the unique 3D porous structure, in which the RGO network can guarantee the high conductivity of the composite, accommodate the volume change of CoS_2 particles during cycling, and shorten the diffusion lengths for lithium ions. The 3DCG composite can be a promising anode candidate for high-performance lithium-ion batteries.

Keywords: CoS_2, graphene, three-dimensional architecture, lithium ion battery.

1. Introduction

Lithium-ion batteries have been widely investigated due to their increasing applications in portable devices, electronic vehicles and hybrid electronic vehicles.[1-3] The commercial graphite anode with a low theoretical capacity of 372 mAh g^{-1} cannot meet the demands for next-generation anode with higher capacity, better cyclic stability and rate capability. Transitional metal oxides and transitional metal sulfides have been widely investigated due to their high theoretical capacities.[4-6] Among them, CoS_2 has drawn particular research interest due to its high theoretical capacity of 870mAh g^{-1}.[7] However, the application of CoS_2 electrode is hindered by several problems. For example, the pulverization of CoS_2 caused by severe volume change during charge/discharge process and the dissolution of the polysulfide intermediate in electrolyte will lead to the fast capacity fading of CoS_2 electrode.[8, 9]

To address such issues, several strategies have been developed. Previous works in transition metal sulfides and transition metal oxides anodes have shown that using nanostructured materials is an effective way to solve such issues, for nanostructured materials possess several advantages over their bulky counterparts.[10-13] Firstly, nanostructured materials have shorter lithium ions diffusion paths. Secondly, the designed nanostructured materials display more accommodation to the strain of the lithiation/delithiation, which is good for preserving electrode structural integrity. Finally, the nanostructured materials have larger electrode/electrolyte contact area that is beneficial for the high current rate performance. For instance, hollow spheres of CoS_2, worm-like CoS_2, yolk-shell spheres of CoS_2 and ultrasmall particles of CoS_2 exhibit improved electrochemical performances compared to the bulky samples.[8, 14-16] Another effective method is to use conductive carbon materials to accommodate the volume change, improve the conductivity of electrode and trap the

polysulfide, leading to enhance the electrochemical properties of CoS_2.[8, 16-18] In particular, two-dimensional (2D) graphene is a promising material to combine with transition metal oxides and transition metal sulfides, due to its superior electronic conductivity, large surface area, good flexibility, excellent chemical and thermal stability. Recently, it was revealed that 3D graphene network assembled by 2D graphene sheets not only possesses the intrinsic properties of 2D graphene sheets, but also can provide the resultant graphene-based composites with strong mechanical strengths, large electrode/electrolyte contact area and short path lengths for lithium ions.[4, 19, 20] For example, the properties of transition metal oxides or transition metal sulfides have been significantly enhanced after combining with 3D graphene network.[21-24] It is expected that the composite anode consisting of CoS_2 and 3D graphene network will possess good electrochemical performances. However, to our best knowledge, there are still no reports on the synthesis and electrochemical properties of CoS_2 supported on 3D graphene network.

In this study, for the first time, three-dimensional porous architecture of CoS_2/reduced graphene oxide (3DCG) was synthesized via a facile hydrothermal reaction followed by a freeze-drying process. The CoS_2 particles are uniformly anchored on the interconnected 3D graphene network and the composite shows high reversible capacity and good rate capability.

2. Experimental

2.1 Synthesis of 3DCG

In a typical procedure, graphite oxide (GO) was prepared by a modified Hummer's method as reported elsewhere previously.[25, 26] 200 mg of GO was dissolved in 40 mL of deionized (DI) water with sonication for 2 h to form a uniform dispersion. Then 0.38 g of $CoCl_2 \cdot 6H_2O$ was added into the dispersion under stirring. After stirring for 1 h, 20 mL

aqueous solution of thioacetamide (TAA) (15 mg mL^{-1}) was added into the above mixture drop by drop. The mixture was transferred to a 100-mL Teflon-lined stainless steel autoclave, heated up to 180 ^{o}C, and kept for 12 h. After cooling down naturally, the product was washed several times with DI water and then treated by freeze-drying for 24 h.

The control samples were also prepared. Pristine CoS_2 was directly synthesized by $CoCl_2 \cdot 6H_2O$ and TAA following the similar procedures; the RGO was synthesized by GO via the similar procedure without adding cobalt source and sulfur source.

2.2 Characterization

The samples were characterized by X-ray diffraction (XRD Rigaku D/MAX-rA diffractometer) using Cu Kα radiation. Raman spectra were acquired at room temperature with excitation laser lines of 532 nm (Horiba). Thermogravimetric analysis (TGA) was carried out on a TA Instruments TGA-Q50 in the temperature range of 50-700 ^{o}C at a heating rate of 10 ^{o}C min^{-1} in air. The bonding configurations of samples were investigated by using X-ray photoelectron spectroscopy (XPS, Kratos XSAM800, Al Ka radiation (144 W, 12 mA, 12 kV)).The materials were compressed into films at 20 MPa with thickness of ~300 μm and then the electrical conductivity was measured by a standard fourpoint probe resistivity measurement system (SX1944, Suzhou, China). The morphology investigations were examined by scanning electron microscope (SEM，JSM-7000F, JEOL) and transmission electron microscope(TEM, Tecnai F20 at 200 kV).

2.3 Electrochemical measurements

Electrochemical performances of the samples were evaluated in coin-type half cells (CR2025). The specific capacity of 3DCG was calculated based on the total mass of the composite. The working electrodes were made of active materials, carbon black (Super P

Timcal) and poly(vinylidene fluoride) (PVDF) binder with a weight ratio of 80:10:10, using N-methyl-2-pyrrolidinone (NMP) as a dispersant to form a slurry. Then the slurry was spread on the copper foil and dried at 120 ^{o}C in vacuum for 12 h. The average mass loading of electrodes is 1 mg cm^{-1}. The electrodes were then assembled into half cells in an argon-filled MBraun glove box with oxygen and water content below 0.5 ppm, using lithium foil as counter electrode. Celgard 2400 was used as separator. 1 M LiPF6 solution in a 1:1 w/w mixture of ethylene carbonate (EC)/dimethyl carbonate (DMC) was used as the electrolyte. The cells were charged and discharged at various current densities between 0.05 and 3 V vs. Li/Li^{+} by LAND electrochemical workstation. Cyclic voltammetry (CV) experiments and electrochemical impedance spectroscopy (EIS) were performed by CHI660D electrochemical workstation (CHI instrument). CV measurements were performed at a scan rate of 0.5 mV s^{-1} in the voltage range of 50 mV to 3 V. EIS tests were carried out at open-circuit potential in the frequency range between 100 kHz and 0.01 Hz with a perturbation amplitude of 5 mV. All measurements were carried out at room temperature.

3. Results and discussion

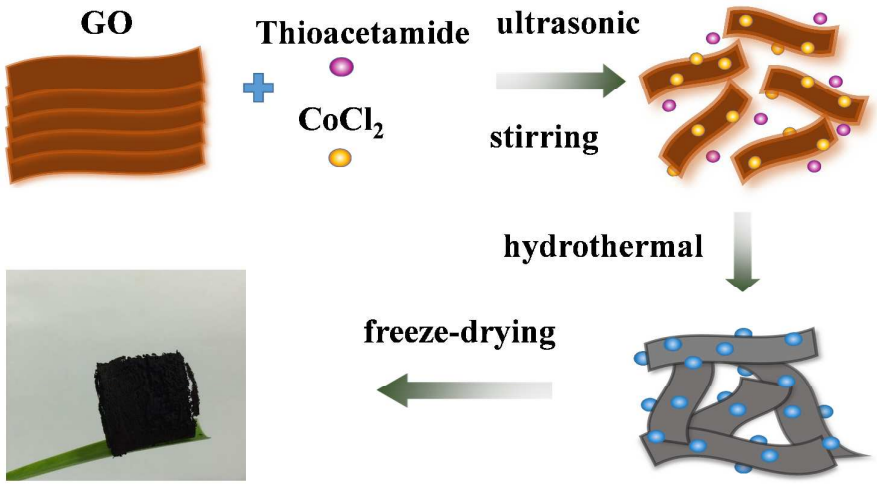

Fig.1 Schematic illustration of the synthesis of 3DCG.

The typical synthesis route is illustrated in Fig. 1. Firstly, the GO sheets can be dispersed in the water due to the strong hydrophilicity and electrostatic repulsion effect. Then, the GO sheets started to be reduced during hydrothermal reaction, and the partially reduced GO sheets became hydrophobic due to the decrease of oxygenated functionalities. With the hydrothermal reaction proceeding, the 3D random stacking of reduced GO sheets was formed with the help of hydrophobicity and π-π stacking. Finally, the increasing hydrophobicity and π-π stacking leaded to form 3D cross-linked RGO network.[27, 28] At the same time, the precursors Co^{2+} absorbed on the surface of GO sheets reacted with the sulfur source and formed CoS_2 particles.[17] After hydrothermal reaction, the composite with CoS_2 particles anchored on RGO network was further treated by freeze-drying to obtained 3DCG.

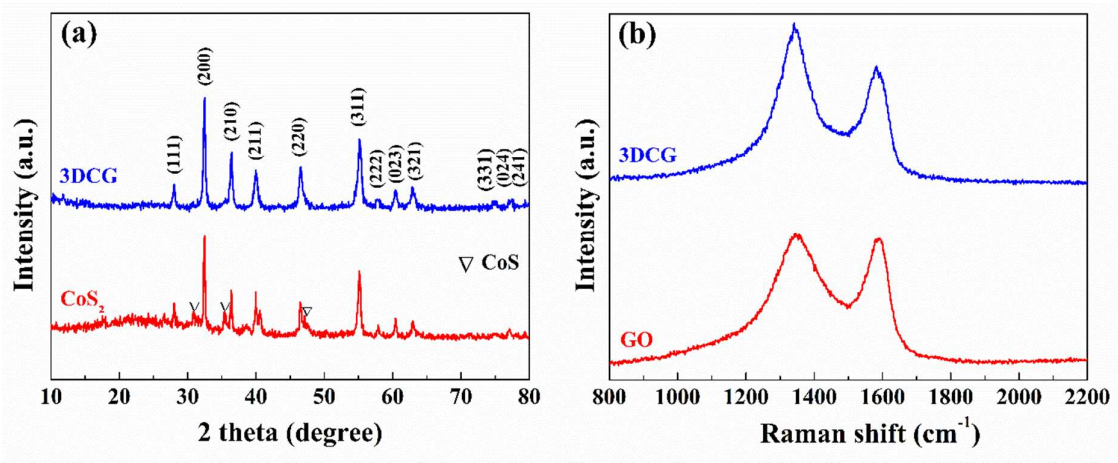

Fig. 2 (a)XRD patterns of CoS_2 and 3DCG. (b)Raman spectra of GO and 3DCG.

The XRD patterns of CoS_2 and 3DCG are shown in Fig. 2a. The 3DCG exhibits a few characteristic peaks with strong intensities, which can be indexed to cubic CoS_2 (PDF no. 89-3056) with a space group of Pa-3 (205).[29] Moreover, in the pattern of 3DCG, the (002) diffraction peak of the graphene nanosheets cannot be detected.[30] Graphene nanosheets will be further characterized by Raman and transmission electron microcopy (TEM). A small

amount of CoS is detected in pristine CoS_2 sample, which is reported by previous research via a similar preparing method.[18] The disappearance of CoS in 3DCG may result from the oxidaztion of GO. The weight fraction of CoS_2 and RGO in 3DCG can be determined to be 70.27 wt% and 29.73 wt%, respectively (Fig. S1).

Fig. 2b shows the Raman spectra of GO and 3DCG. Both samples show two peaks at ~1350 cm^{-1} and ~1580 cm^{-1}, corresponding to the disordered (D) and graphitic (G) bands of graphene. The intensity ratio of the D band to the G band (I_D/ I_G) are 1.03 and 1.31 for GO and 3DCG, respectively. Compared with GO, the higher intensity ratio of 3DCG (I_D/ I_G=1.31) indicates that many defects have formed on the surface of graphene sheets. This is attributed to the reduction of GO and the insertion of CoS_2 particles into graphene sheets which is similar to the intercalation phenomena reported previously.[4, 9, 31, 32] X-ray photoelectron spectroscopy(XPS) spectra of C 1s of GO and RGO are shown in Fig. S2. The peak of C–O bond (286.3 eV) is significantly suppressed after reduced by hydrothermal reaction. The C/O ratio of RGO is about 4.0. Moreover, the electrical conductivity of GO (6.73×10^{-5} S cm^{-1}) was dramatically enhanced up to 1.35 S cm^{-1} (RGO) after hydrothermal reaction. These data suggest that the quality of RGO is good.

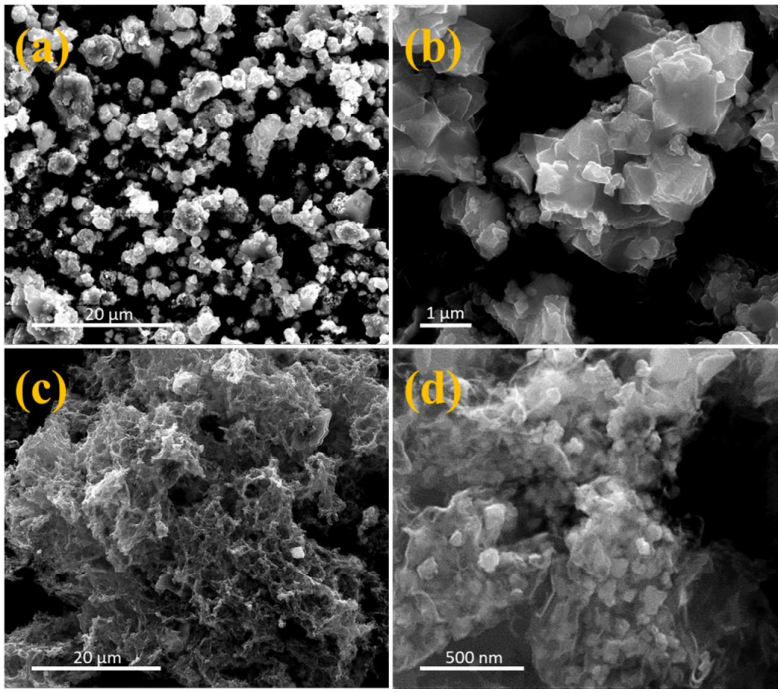

Fig. 3 (a) and (b) SEM images of CoS_2. (c) and (d) SEM images of 3DCG.

The morphologies and microstructures of the pristine CoS_2 and 3DCG were investigated by scanning electron microscopy (SEM). As shown in Fig. 3a and b, the particles of pristine CoS_2 are seriously aggregated with an average size of several micrometers. However, in 3DCG, the structure and morphology are quite different. As shown in Fig. 3c, the composite demonstrates a 3D interconnected network with numerous pores. The porous network was assembled by RGO nanosheets during the hydrothermal process and maintained the structure after freeze-drying. It is noteworthy that the particles are uniformly anchored on graphene sheets in the high-magnification SEM image in Fig. 3d. The small size and the homogenously distribution of CoS_2 particles in 3DCG could be attributed to the functional groups on GO acting as the nucleation sites for CoS_2 particles.[9]

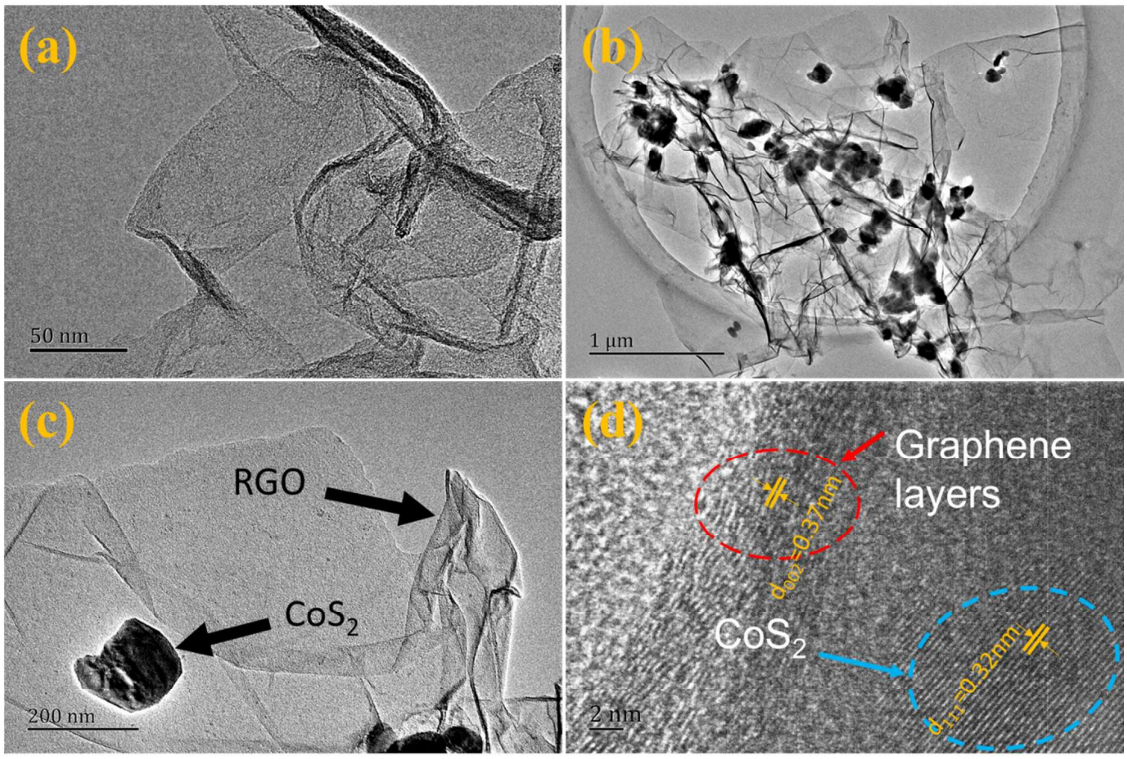

Fig. 4 (a) TEM image of RGO. (b) and (c) TEM images of 3DCG. (d) HRTEM image of 3DCG.

The microstructure of the 3DCG was further investigated by TEM. Fig. 4a presents the typical TEM image of RGO sheets which is ultrathin and wrinkle. For 3DCG, the TEM images illustrate that these CoS_2 particles (with sizes of 150-200 nm) are uniformly anchored on the RGO sheets, as shown in Fig. 4b and c. The high-resolution TEM (HRTEM) image of 3DCG is shown in Fig. 4d. The red circle indicates the RGO sheets with an interplanar spacing of 0.37 nm ((002) plane of graphene), and the blue circle indicates the CoS_2 with a d-spacing of 0.32 nm, which corresponds to the (111) plane of CoS_2.

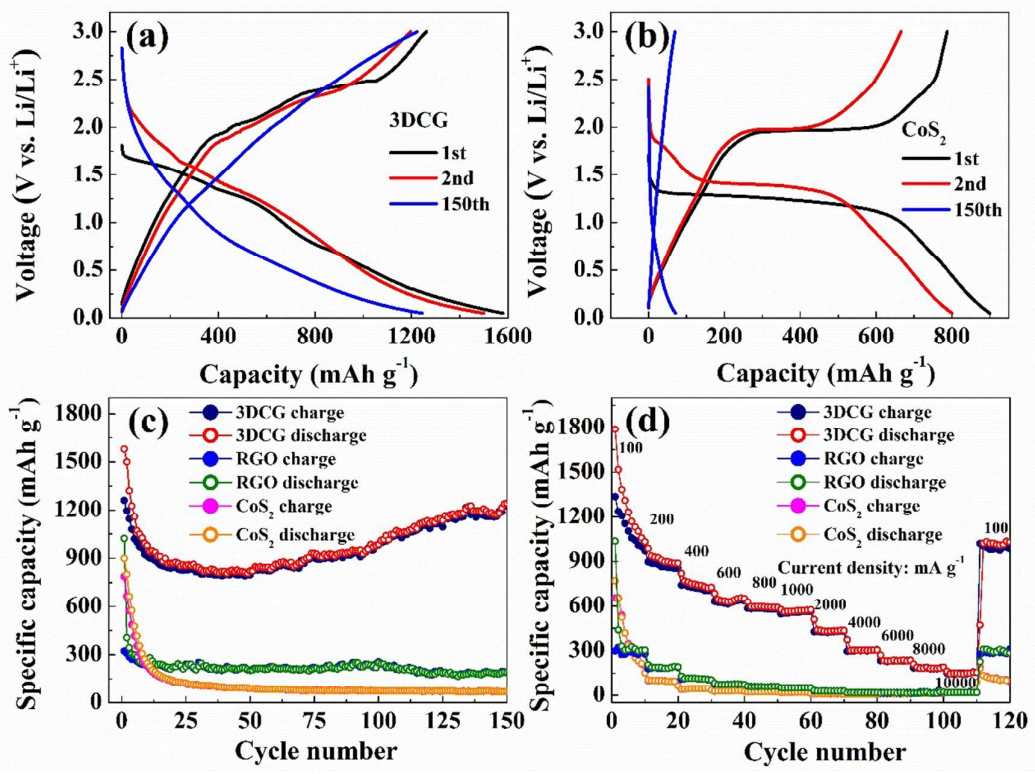

Fig. 5 The galvanostatic charge-discharge curves of (a) 3DCG, (b) CoS_2 at 100 mA g^{-1}. (c) Cyclic and (d) rate performance of CoS_2, RGO and 3DCG.

The electrochemical properties of the CoS_2, RGO and 3DCG were examined by 2025 coin cells. Fig. 5a shows the 1st, 2nd and 150th discharge and charge profiles of 3DCG cycled at a current density of 100 mA g^{-1} in the range of 0.05-3.0 V vs. Li/Li^+. In first discharge curve, there are three plateaus (1.5, 1.3 and 0.8 V). The plateaus at 1.5 and 1.3 V shift to 1.7 and 1.3 V in subsequent cycles, respectively. The plateau at 0.8 V is related to the foramtion of solid electrolyte interface (SEI) film.[16] In subsequent cycles, the plateau at 1.7 V is attributed to the initial small amount insertion of lithium ions reaction: $CoS_2 + x Li^+ + x e^- \rightarrow Li_xCoS_2$. The plateau at 1.3 V is corresponding to the reaction: $Li_xCoS_2 + (4-x)Li^+ + (4-x)e^- \rightarrow Co + 2Li_2S$. In charge curves, the plateaus at ~2.0 and 2.4 V are attributed to the delithiation process.[33] The CV curves of 3DCG have been recorded (Fig. S3). As shown in Fig. S3, the peaks at the first two sweeps are not very typical CoS_2-based peaks, which may result from

the unstable electrochemical reactions during the first two sweeps. One can see that after 20 cycles, the CV curves tend to be stable. This is also consistent with the cycling performance of the 3DCG anode (Fig. 5c). The 3DCG electrode delivers the initial discharge and charge capacities of 1579 and 1261 mAh g^{-1}, respectively, giving a Coulombic efficiency of 79.9%. The irreversible capacity loss might result from the inevitable decomposition of electrolyte and the formation of SEI film, which has been reported in transition metal oxide and transition metal sulfide based anode materials.[34, 35] However, the pristine CoS_2 exhibits much lower discharge and charge capacity, as shown in Fig. 5b.

It is noted that the reversible capacity of 3DCG (1499 mAh g^{-1}) is much higher than the theoretical value of CoS_2 (870 mAh g^{-1}). The extra capacity may be attributed probably to two factors. Firstly, the nanomaterials of anode usually display higher capacities than those of bulk materials or materials with large size. The nanostructured material can provide more active sites for electrochemical reaction,[36, 37] which can effectively enhance the reversible capacity.[15] Secondly, the presence of highly conductive RGO in 3DCG might enhance the reversible capacity. Although the capacity of RGO itself is not very high, the conductive RGO network can serve as the pathways for electrons and lithium ions and improve the conductivity of electrode, which can improve the reversible capacity.[38, 39]

The cyclic performances of CoS_2, RGO and 3DCG at a current of 100 mA g^{-1} are plotted in Fig. 5c. It is clear that 3DCG demonstrates an outstanding cyclic performance. After 150 cycles, a high capacity of 1245 mAh g^{-1} can be retained for 3DCG, while the capacities of 190 and 71 mAh g^{-1} are retained for RGO and pristine CoS_2, respectively. The decrease in capacity for the first 20 cycles is not rare for the electrode materials with volume effect.[17, 40] This phenomenon could be attributed to the specific electrode evolution process of CoS_2

anode material.[33] During the first charge cycle, the CoS_2 will react with lithium ions to transform into Co and Li_2S.[41] The sudden appearance of abundant Li_2S will block the further lithium ions transfer between electrode materials and electrolyte leading to the capacity fading. With the electrochemical cycles proceeding, 3DCG becomes more porous, which provides tunnels for the electrolyte to access the inner part of the active materials. Therefore, the trapped active materials can expose to the electrolyte again and release lithium ions, thus ending the capacity decay after ~20 cycles.

The capacity of 3DCG after 150 cycles in this study is the highest ever reported in CoS_2-based anodes, as shown in Fig. S4.[7, 8, 14-17, 33, 41-44] The improvement of cycling stability can be attributed to the intrinsic advantages of graphene which can not only effectively mitigate the volume changes and maitain the structural integrity even afer 150 cycles (Fig. S5),[9, 45] but also traps the polysulfides dissolved in the electrolyte.[9, 45, 46] The reversible capacity of 3DCG increases continuously after ~50 cycles. The phenomenon of capacity increasing in CoS_2-based anode material is not an exception.[17] Generally, this phenomenon can be attributed to the growth and dissolution of a gel-like polymer film which is related to the extra capacity of transition metal oxides or transition metal sulfides in the low potential region.[12, 17, 47-51] The reversible formation and decomposition of the gel-like polymer film can provide interfacial storage for extra lithium ions through the pseudocapacitive behavior.[47-49] The gel-like polymer film is beneficial to the long-term cyclic performance and leads to the increasing capacity after 50 cycles.

Fig. 5d demonstrates the rate performances of the three electrodes at various current denisities. The 3DCG delivers capacities of ~950 mAh g^{-1}, 750 mAh g^{-1}, 570 mAh g^{-1}, 306 mAh g^{-1} and 150 mAh g^{-1} at 200 mA g^{-1}, 400 mA g^{-1}, 1000 mA g^{-1}, 4000 mA g^{-1} and 10000

mA g^{-1}, respectively. When the current density is returned back to100 mA g^{-1}, the capacity is able to recover to the initial level at 100 mA g^{-1} (~1000 mAh g^{-1}), which indicates a much better rate capability than those of bare RGO and pristine CoS_2. The good rate capability of the 3DCG results from the incorporation of uniformly dispersed CoS_2 particles and interconnected 3D graphene network. On the one hand, the graphene nanosheets with superior electronic conductivity and high surface area can provide an ideal 3D conductive matrix for the active material particles and more available area for electrolyte access. On the other hand, the feature of highly dispersed CoS_2 particles with small size on graphene sheets can decrease the diffusion lengths for lithium ions during charge/discharge process.

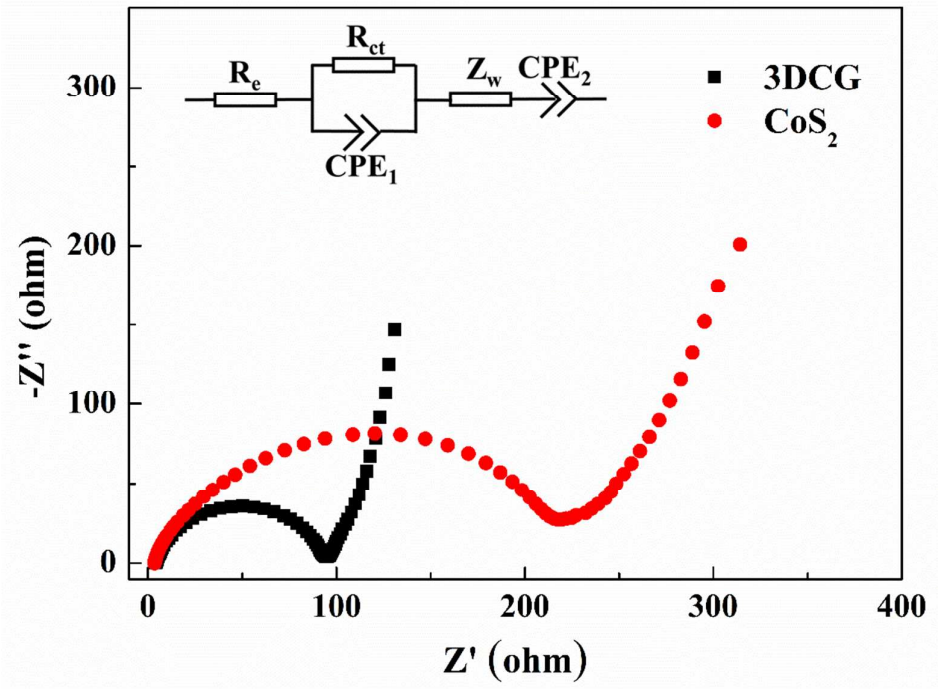

Fig. 6 Nyquist plots of CoS_2 and 3DCG.

To further understand the enhanced performance of 3DCG, electrochemical impedance spectroscopy (EIS) was carried out with fresh cells and the Nyquist plots of 3DCG and pristine CoS_2 are shown in Fig. 6. The semicircle in the Nyquist plots could be attributed to the charge-transfer process and the inclined line in the low-frequency region is assigned to

lithium ions diffusion. R_e represents the internal resistance of the cell; R_{ct} and CPE_1 denote for the charge-transfer resistance and constant phase element of the electrode/electrolyte interface, respectively; Z_w is referred to the Warburg impedance, and CPE_2 is associated with active mass capacitance. According to the fitting results, the R_{ct} of 3DCG is 88 Ω which is much smaller than that of CoS_2 (R_{ct}= 208 Ω). The improved electrochemical reaction kinetic can lead to excellent electrochemical performance of 3DCG.

Conclusion

In summary, three-dimensional porous 3DCG architecture has been synthesized by a facile hydrothermal reaction and subsequent freeze-drying process. The 3DCG demonstrates outstanding electrochemical performances. The unique porous 3D graphene interconnected network can guarantee the high conductivity of the composite, accommodate the volume change of CoS_2 particles during cycling, absorb the polysulfides and shorten the diffusion lengths for lithium ions and electrons. Those properties of 3DCG result in the excellent electrochemical performances: the reversible discharge capacity is as large as 1499 mAh g^{-1} which is the highest ever reported for CoS_2-based materials; the rate capability remains 306 mAh g^{-1} even at 4000 mA g^{-1}. The outstanding electrochemical properties of 3DCG suggest that this material is a promising anode material for next generation lithium-ion batteries.

Acknowledgments

The research was supported by the National Natural Science Foundation of China (Grant No. 51202022, 51372033 and 61378028), the National High Technology Research and Development Program of China (Grant No. 2015AA034202), the 111 Project (Grant No. B13042), the Sichuan Youth Science and Technology Innovation Research Team Funding (Grant No. 2011JTD0006), the International Science and Technology Cooperation Program of

China (Grant No. 2012DFA51430), and the Sino-German Cooperation PPP Program of China.

References

1. M. Wakihara, *Mater. Sci. Eng., R*, 2001, **33**, 109-134.
2. L. Lu, X. Han, J. Li, J. Hua and M. Ouyang, *J. Power Sources*, 2013, **226**, 272-288.
3. H. Li, Z. Wang, L. Chen and X. Huang, *Adv. Mater.*, 2009, **21**, 4593-4607.
4. W. Chen, S. Li, C. Chen and L. Yan, *Adv. Mater.*, 2011, **23**, 5679-5683.
5. Y. Liu, X. Zhu, Z. Duan and X. Xie, *Chem. Commun.*, 2013, **49**, 10305-10307.
6. Z. Duan, Y. Sun, Y. Liu, X. Xie and X. Zhu, *RSC Adv.*, 2014, **4**, 41543-41550.
7. J. M. Yan, H. Z. Huang, J. Zhang, Z. J. Liu and Y. Yang, *J. Power Sources*, 2005, **146**, 264-269.
8. Q. Wang, R. Zou, W. Xia, J. Ma, B. Qiu, A. Mahmood, R. Zhao, Y. Yang, D. Xia and Q. Xu, *Small*, 2015, **11**, 2511-2517.
9. B. Qiu, X. Zhao and D. Xia, *J. Alloys Compd.*, 2013, **579**, 372-376.
10. A. S. Aricò, P. Bruce, B. Scrosati, J. Tarascon and W. van Schalkwijk, *Nat. Mater.*, 2005, **4**, 366-377.
11. L. Pan, K. Wang, X. Zhu, X. Xie and Y. Liu, *J. Mater. Chem. A*, 2015, **3**, 6477-6483.
12. L. Pan, X. Zhu, X. Xie and Y. Liu, *J. Mater. Chem. A*, 2015, **3**, 2726-2733.
13. X. Zhu, K. Wang, D. Yan, S. Le, R. Ma, K. Sun and Y. Liu, *Chem. Commun.*, 2015, **51**, 11888-11891.
14. Q. Wang, L. Jiao, Y. Han, H. Du, W. Peng, Q. Huan, D. Song, Y. Si, Y. Wang and H. Yuan, *J. Phys. Chem. C*, 2011, **115**, 8300-8304.
15. R. Jin, L. Yang, G. Li and G. Chen, *J. Mater. Chem. A*, 2015, **3**, 10677-10680.
16. W. Qiu, J. Jiao, J. Xia, H. Zhong and L. Chen, *Chem. Eur. J.*, 2015, **21**, 4359-4367.
17. J. Xie, S. Liu, G. Cao, T. Zhu and X. Zhao, *Nano Energy*, 2013, **2**, 49-56.
18. Z. X. Huang, Y. Wang, J. I. Wong, W. H. Shi and H. Y. Yang, *Electrochim. Acta*, 2015, **167**, 388-395.
19. M. Pumera, *Energy Environ. Sci.*, 2011, **4**, 668-674.
20. W. Chen and L. Yan, *Nanoscale*, 2011, **3**, 3132-3137.
21. X. Zhu, P. Zhang, S. Xu, X. Yan and Q. Xue, *ACS Appl. Mater. Interfaces*, 2014, **6**, 11665-11674.
22. B. Qiu, M. Xing and J. Zhang, *J. Am. Chem. Soc.*, 2014, **136**, 5852-5855.
23. X. Cao, Y. Shi, W. Shi, X. Rui, Q. Yan, J. Kong and H. Zhang, *Small*, 2013, **9**, 3433-3438.
24. X. Jiang, X. Yang, Y. Zhu, J. Shen, K. Fan and C. Li, *J. Power Sources*, 2013, **237**, 178-186.
25. J. He, Y. Chen, P. Li, Z. Wang, F. Qi and J. Liu, *RSC Adv.*, 2014, **4**, 2568-2572.
26. Z. Wang, P. Li, Y. Chen, J. He, B. Zheng, J. Liu and F. Qi, *Mater. Lett.*, 2014, **116**, 416-419.
27. Z. Han, Z. Tang, P. Li, G. Yang, Q. Zheng and J. Yang, *Nanoscale*, 2013, **5**, 5462-5467.
28. Y. Xu, K. Sheng, C. Li and G. Shi, *ACS Nano*, 2010, **4**, 4324-4330.
29. N. Elliott, *J. Chem. Phys.*, 1960, **33**, 903.
30. Y. Zhang, J. Xie, T. Zhu, G. Cao, X. Zhao and S. Zhang, *J. Power Sources*, 2014, **247**, 204-212.
31. T. H. Bointon, I. Khrapach, R. Yakimova, A. V. Shytov, M. F. Craciun and S. Russo, *Nano Lett.*, 2014, **14**, 1751-1755.
32. Y. Gu, Y. Xu and Y. Wang, *ACS Appl. Mater. Interfaces*, 2013, **5**, 801-806.
33. J. Guo, F. Li, Y. Sun, X. Zhang and L. Tang, *Electrochim. Acta*, 2015, **167**, 32-38.
34. C. S. Rout, B. Kim, X. Xu, J. Yang, H. Y. Jeong, D. Odkhuu, N. Park, J. Cho and H. S. Shin, *J. Am. Chem. Soc.*, 2013, **135**, 8720-8725.
35. X. Hou, X. Wang, B. Liu, Q. Wang, Z. Wang, D. Chen and G. Shen, *ChemElectroChem*, 2014, **1**, 108-115.
36. E. Garand, M. Z. Kamrath, P. A. Jordan, A. B. Wolk, C. M. Leavitt, A. B. McCoy, S. J. Miller and M. A.

Johnson, *Science*, 2012, **335**, 698-702.

37. X. Cao, Y. Shi, W. Shi, X. Rui, Q. Yan, J. Kong and H. Zhang, *Small*, 2013, **9**, 3433-3438.

38. P. Guo, H. Song, X. Chen, L. Ma, G. Wang and F. Wang, *Anal. Chim. Acta*, 2011, **688**, 146-155.

39. H. Wang, L. Cui, Y. Yang, H. Sanchez Casalongue, J. T. Robinson, Y. Liang, Y. Cui and H. Dai, *J. Am. Chem. Soc.*, 2010, **132**, 13978-13980.

40. J. Guo, L. Chen, G. Wang, X. Zhang and F. Li, *J. Power Sources*, 2014, **246**, 862-867.

41. Q. Su, J. Xie, J. Zhang, Y. Zhong, G. Du and B. Xu, *ACS Appl. Mater. Interfaces*, 2014, **6**, 3016-3022.

42. G. Huang, T. Chen, Z. Wang, K. Chang and W. Chen, *J. Power Sources*, 2013, **235**, 122-128.

43. Y. Wang, J. Wu, Y. Tang, X. Lü, C. Yang, M. Qin, F. Huang, X. Li and X. Zhang, *ACS Appl. Mater. Interfaces*, 2012, **4**, 4246-4250.

44. W. Luo, Y. Xie, C. Wu and F. Zheng, *Nanotechnology*, 2008, **19**, 75602.

45. L. Fei, Q. Lin, B. Yuan, G. Chen, P. Xie, Y. Li, Y. Xu, S. Deng, S. Smirnov and H. Luo, *ACS Appl. Mater. Interfaces*, 2013, **5**, 5330-5335.

46. H. Wang, Y. Yang, Y. Liang, J. T. Robinson, Y. Li, A. Jackson, Y. Cui and H. Dai, *Nano Lett.*, 2011, **11**, 2644-2647.

47. S. Laruelle, S. Grugeon, P. Poizot, M. Dolle´, L. Dupont and J. Tarascon, *J. Electrochem. Soc.*, 2002, **149**, A627-A634.

48. S. Grugeon, S. Laruelle, L. Dupont and J. M. Tarascon, *Solid State Sci.*, 2003, **5**, 895-904.

49. A. Ponrouch, P. Taberna, P. Simon and M. R. Palacín, *Electrochim. Acta*, 2012, **61**, 13-18.

50. L. Pan, X. Zhu, X. Xie and Y. Liu, *Adv. Funct. Mater.*, 2015, **25**, 3341-3350.

51. D. Wang, J. Yang, X. Li, D. Geng, R. Li, M. Cai, T. Sham and X. Sun, *Energy Environ. Sci.*, 2013, **6**, 2900-2906.

Graphical abstract

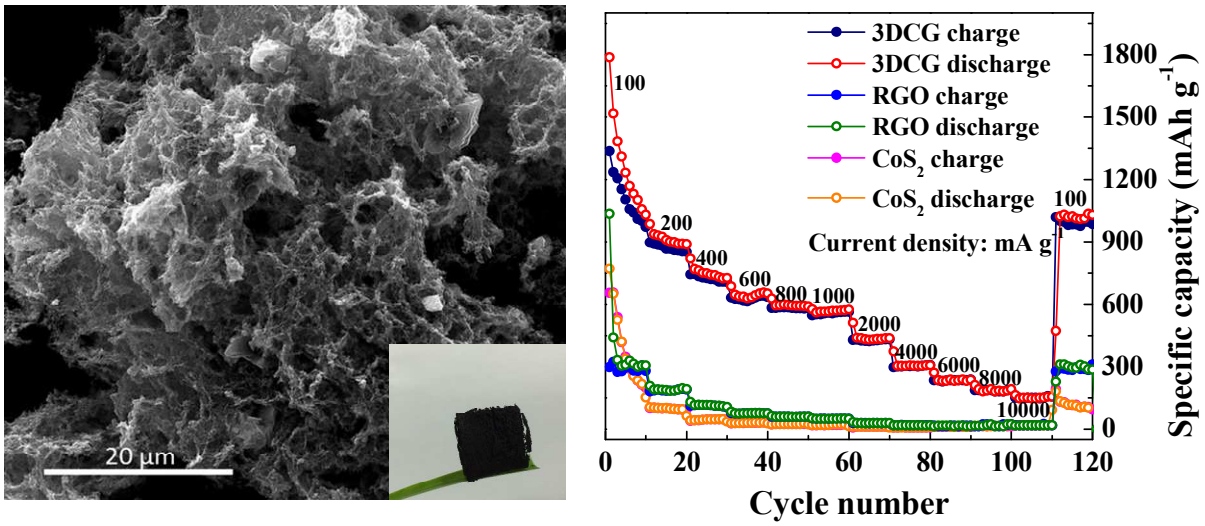

The porous three-dimensional CoS_2/RGO (3DCG) anode exhibits outstanding cyclic stability, high specific capacity, and excellent high-rate performance.